

1                   **Compound Flooding in Convergent Estuaries:**  
2                   **Insights from an Analytical Model**

3  
4  
5                   Ramin Familkhalili<sup>1</sup>, Stefan A. Talke<sup>2</sup>, and David A. Jay<sup>3</sup>

6                   <sup>1</sup>Department of Civil and Environmental Engineering, Old Dominion University, Norfolk, VA, USA

7                   <sup>2</sup>Department of Civil and Environmental Engineering, California Polytechnic State University, San Luis Obispo, CA, USA

8                   <sup>3</sup>Department of Civil and Environmental Engineering, Portland State University, Portland, OR, USA

9  
10  
11  
12  
13  
14                  Correspondence to: Ramin Familkhalili (rfamilkh@odu.edu)

## 24 Key Points

- 25 • An idealized analytical model shows that deepening an estuarine channel reduces the  
26 impacts of river flow on peak water level but increases the effects of storm tide.
- 27 • A friction number shows the competing effects of surge time scale, depth, and convergence  
28 on water level amplitudes.
- 29 • Channel deepening changes the balance of fluvial and coastal flood risks and moves the  
30 crossover between storm tide vs. fluvial-dominated flooding landward.

## 31 **Abstract**

32 We investigate here the effects of geometric properties (channel depth and cross-sectional  
33 convergence length), storm surge characteristics, friction, and river flow on the spatial and  
34 temporal variability of compound flooding along an idealized, meso-tidal coastal-plain estuary.  
35 An analytical model is developed that includes exponentially convergent geometry, tidal forcing,  
36 constant river flow, and a representation of storm surge as a combination of two sinusoidal waves.  
37 Non-linear bed friction is treated using Chebyshev polynomials and trigonometric functions, and  
38 a multi-segment approach is used to increase accuracy. Model results show that river discharge  
39 increases the damping of surge amplitudes in an estuary, while increasing channel depth has the  
40 opposite effect. Sensitivity studies indicate that the impact of river flow on peak water level  
41 decreases as channel depth increases, while the influence of tide and surge increases in the  
42 landward portion of an estuary. Moreover, model results show less surge damping in deeper  
43 configurations and even amplification in some cases, while increased convergence length scale  
44 increases damping of surge waves with periods of 12 -72 h. For every modeled scenario, there is  
45 a point where river discharge effects on water level outweigh tide/surge effects. As a channel is  
46 deepened, this cross-over point moves progressively upstream. Thus, channel deepening may alter  
47 flood risk spatially along an estuary and reduce the length of a river-estuary, within which fluvial  
48 flooding is dominant.

## 49 **Plain language summary**

50 Storm surge, tides, and high river flow often combine to cause flooding in estuaries, a problem  
51 known as compound flooding. In this study, we investigate these factors and how changes to  
52 estuary and river geometry influence peak water levels. Our results show that surge waves become  
53 larger when the depth of a shipping channel is increased, for example due to dredging or sea-level  
54 rise. The same deepening, however, reduces the effect of river flow on peak water level. The result  
55 is that the region over which river influence dominates the peak water level moves upstream as a  
56 system becomes deeper. This change in the ‘cross-over location’ reduces the domain over which  
57 river flooding is the dominant consideration. This study offers an analytical framework for  
58 reducing river-estuary flood risk by better understanding of how bathymetry, surge time scale, and

59 river discharge affect surge and tidal amplitudes, and therefore flood heights and inundation, in  
60 these systems.

61 Keywords: Analytical model, Compound flooding, Estuary, Surge, Tide

## 62 **1- Introduction**

63 Understanding tidal, surge, and river flow dynamics, and how they combine and interact to produce  
64 the maximum or total water level (TWL), is important for emergency planning and as an aspect of  
65 wave dynamics. It is also a problem that is changing rapidly, as sea-level rises and systems are  
66 altered by engineering. This contribution analyzes, therefore, the relative influence of river flow  
67 and storm surge effects along the river-estuary continuum from a dynamical perspective that  
68 enables us to assess the effects of non-linear interactions, geometry, and changing (time varying)  
69 conditions.

70 Many low-lying coastal and riverine areas have been affected by combined coastal and riverine  
71 floods over the last few decades (e.g., Jongman et al., 2012; Nicholls et al., 2007). In cases such  
72 as Hurricane Harvey (Gulf of Mexico, August 2017), flooding was driven primarily by  
73 precipitation and runoff (van Oldenborgh et al., 2017; Wang et al., 2018). Other flood events, such  
74 as Hurricane Sandy, were forced by the combined effects of tide and storm surge, i.e., by “storm  
75 tides” the sum of storm surge and tidal water level (Orton et al., 2016). Some storm events, like  
76 Hurricanes Irene and Irma, produce both coastal and inland flooding because both storm surge and  
77 river flow produce elevated coastal water levels in a spatially varying pattern (e.g., Orton et al.,  
78 2012; Ralston et al., 2013; Talke et al., 2021). Accordingly, a flood influenced by both storm tide  
79 and precipitation run-off is a ‘compound flood’ (Zscheischler et al., 2018; Wahl et al., 2015). The  
80 relative timing of the coastal and fluvial forcing, and the time scale over which water levels are  
81 elevated, matters in terms of impact (e.g., Zheng et al., 2014). Storm surge flooding generally  
82 occurs first and for a shorter period (time scales of hours to a day or two) than river flooding,  
83 which may last for weeks or even months, particularly in regions with a large watershed and flat  
84 topography (e.g., Johnson et al., 2016, Wong et al., 2014). The timing of storm surge relative to  
85 tidal high-water (Famalkhalili and Talke, 2016) or the spring-neap tidal cycle also influences flood  
86 heights, even upstream of tidal influence (Helaire et al., 2020).

87 The spatial variability of compound flooding is influenced by the geometry of an estuary and may  
88 change over time due to system alterations, including channel deepening, sea-level rise, and  
89 wetland reclamation (Ralston et al., 2019; Helaire et al., 2019, 2020). Recent studies have shown  
90 that human-caused changes to the geometry of estuaries affect the dynamics of long-waves (see  
91 reviews by Talke and Jay, 2020, and Jay et al., 2021), with tidal range in some regions more than  
92 doubling (e.g., Winterwerp et al., 2013). Similar effects are observed with storm surge; for  
93 example, doubling the depth of the shipping channel in the Cape Fear Estuary was modeled to  
94 increase the magnitude of a worst-case scenario storm surge in Wilmington (NC) from  $3.8 \pm 0.25$

95 m to  $5.6 \pm 0.6$  m (Familkhalili and Talke, 2016). By contrast, depth increases may cause the mean  
96 water level in tidal rivers to drop, due to decreased frictional effects (Jay et al., 2011; Helaire et  
97 al., 2019); hence, flood risk in Albany (NY) has significantly dropped over the past 150 years,  
98 despite a doubling of tide range and an increase in storm surge magnitudes (Ralston et al., 2019).  
99 Closer to the coast, flood hazard within the same estuary markedly increased over the same time  
100 period (e.g., Talke et al., 2014). Hence, evolution of flood hazard can be spatially variable, to an  
101 extent that is just beginning to be quantified.

102 Here, an idealized approach is used, which enables a large parameter space to be assessed and the  
103 following two dynamical questions to be investigated:

- 104 a) What factors determine the region in which river flow effects or tide/surge effects dominate  
105 the total water level?
- 106 b) How does the transition from coastal to fluvial dominance shift as geometry changes or as  
107 properties of storm surge (e.g., time scale and magnitude) and river flow (magnitude)  
108 change?

109 We combine a three-sinusoidal wave analytical model based on Jay (1991) with the multi-wave  
110 and multi-segment approach of Giese and Jay (1989) (see Familkhalili et al., 2020 for details) to  
111 quickly query a parameter space or relevant factors and provide insight into how factors such as  
112 storm time scale and the relative magnitudes of different forcing factors influence the dynamics of  
113 compound flooding.

## 114 **2- Methods**

115 Both, analytical solutions and numerical models are regularly used to explore the mechanism of  
116 surge and tidal waves propagation along an estuary (see Talke and Jay, 2020 review). While  
117 numerical models can simulate tidal wave propagation more accurately than analytical models  
118 considering the measurements in a real system, numerical models are typically calibrated for an  
119 existing bathymetric, meteorological, and boundary forcing configurations (e.g., Brandon et al.,  
120 2014; Bertin et al., 2012; Orton et al., 2012). On the other hand, idealized numerical models with  
121 simplified configurations can be used to develop sensitivity studies to investigate the effects of  
122 changing hydrodynamic variables on surge and tidal wave interactions in a system (e.g., Shen and  
123 Gong, 2009; Familkhalili and Talke, 2016), but a downside of these numerical approach is that  
124 studying an entire parameter space is computationally expensive. In contrast, analytical models  
125 rely on fundamental underlying physics and are transparent. Thus, they are good tools to explain  
126 some of the factors (e.g., channel depth, convergence length, river discharge, and surge amplitude  
127 and time scale changes) that alter flood levels in an estuary.

128 We apply an analytical approach to investigate the TWL caused by river discharge, tides, and surge  
129 in an idealized estuary. Various forms of one-dimensional analytical solutions of tidal wave

130 propagation have long been used for idealized and real estuaries (e.g., Dronkers, 1964; Prandle  
131 and Rahman, 1980; Jay, 1991; Friedrichs and Aubrey, 1994; Savenije, 1998; Lanzoni and  
132 Seminara, 1998; Godin, 1999). More complex idealized tidal models investigate overtide  
133 generation and evolution (e.g., Chernetsky et al., 2010), the effects of variable cross-section and  
134 bottom slope (e.g., Savenije et al., 2008, Kästner et al., 2019), and the effects of multiple tidal  
135 constituents and river discharge (Giese and Jay, 1989; Buschman et al., 2009). Other studies have  
136 used a tidal model combined with regression analysis (e.g., Godin, 1999; Kukulka and Jay, 2003a)  
137 to investigate river discharge effects. Such idealized models, by the parameter space analyzed, can  
138 be used to obtain fundamental insights into how long waves in estuaries are affected by depth,  
139 convergence, friction, and boundary forcing.

140 In our approach, we develop an analytical model which is driven by three sinusoidal constituents  
141 and a constant river discharge. Our approach idealizes storm surge as the sum of two sinusoids,  
142 and neglects factors, such as the potential role of wetlands and the floodplain, in order to gain  
143 insight into some of the important, along-channel factors that govern the system response to a  
144 compound event. Similarly, we neglect processes such as Coriolis acceleration, wind waves, and  
145 gravity waves, and focus on the specific case of an incident long-wave that propagates from the  
146 coast in the landward direction and is eventually completely damped out. Though a reflected wave  
147 is produced by convergent geometry in analytical models (Jay, 1991), we neglect the partial  
148 reflections caused by depth and width changes, and do not consider the case of a reflective  
149 upstream boundary. Such factors are important for tidal changes in many estuaries, particular  
150 locations that are near resonance such as the Ems (see Ensing et al., 2015) or near where total  
151 reflections occur (see Ralston et al., 2019). Moreover, we simplify our approach by considering  
152 only constant river flow conditions, a valid approximation for situations in which the time scale of  
153 a river flood event is much longer than a storm surge. These simplifications enable a solution that  
154 is much faster than numerical models and enables a tractable sensitivity study of storm surge and  
155 river flow effects on water levels for different depths, convergence, and boundary conditions.

## 156 **2-1- Analytical model**

157 We use an idealized one-dimensional analytical model developed by Familkhalili et al., (2020) to  
158 investigate how combinations of tides, storm surge, and river flow affect water levels in an estuary.  
159 In this model, storm surge is approximated as the sum of a primary and a secondary sinusoidal  
160 wave. A third sinusoidal frequency is reserved for the  $M_2$  tidal constituent. The resulting model is  
161 conceptually similar to the multi-tide constituent model developed by Giese and Jay (1989) and  
162 the three-wave model of Buschman et al., (2009), with the distinction that two of the waves are  
163 based on the amplitude and timescales of meteorologically induced storm surge rather than an  
164 astronomical tide with a known frequency. Also, the Giese and Jay (1989) model used the  
165 dynamical analysis of Dronkers (1964), that does not correctly include convergence effects,  
166 whereas our model follows the Jay (1991) treatment that includes friction, convergence, and river  
167 inflow.

168 One-dimensional long wave propagation along an idealized, funnel-shaped estuary is described by  
 169 the cross-sectionally integrated equations of mass and momentum conservation (e.g., Jay, 1991;  
 170 Kukulka and Jay, 2003a; Familkhalili et al., 2020):

$$171 \quad \frac{\partial Q}{\partial t} + \frac{\partial}{\partial x} \left( \frac{Q^2}{A} \right) + gA \frac{\partial \xi}{\partial x} + bK = 0 \quad (1)$$

$$172 \quad \frac{\partial Q}{\partial x} + b \frac{\partial \xi}{\partial t} = 0 \quad (2)$$

173 where  $Q$  is cross-sectionally integrated flow ( $m^3s^{-1}$ ) and is the summation of the river and tidal  
 174 transports ( $Q_R + Q_T$ ),  $t$  is time (s),  $x$  is the longitudinal coordinate measured in landward  
 175 direction (m) (see Fig. 1a),  $b$  is width (m),  $g$  is the acceleration due to gravity ( $9.81 ms^{-2}$ ),  $A$  is  
 176 channel cross-sectional area ( $m^2$ ),  $\xi$  is tidal amplitude (m),  $K$  is the bed stress divided by water  
 177 density ( $m^2s^{-2}$ ) ( $\frac{\tau}{\rho} = C_d|u|u$ ),  $C_d$  is a dimensionless drag coefficient, and  $u = Q/A$  is the velocity  
 178 ( $ms^{-1}$ ). The absolute value of  $u$  is assigned to preserve the directionality of stress. For simplicity,  
 179 depth is assumed constant and channel width is allowed to vary exponentially with respect to the  
 180 longitudinal coordinate  $x$  (i.e.,  $b(x) = B_c + (B_0 - B_c)e^{-\frac{x}{L_e}}$ , see Fig. 1a), where  $B_0$  is the width at  
 181 the estuary mouth (m) and  $B_c$  is the constant upstream river width (m) and  $L_e$  is the convergence  
 182 length scale (m) that is the length over which the width decreases by a factor of  $e$ . Following  
 183 Familkhalili et al (2020), we set  $B_0=5$  km and assume that the estuary section of the model domain  
 184 is 1.5 times the convergence length which determine a constant river width of  $\sim 1100$  m. The  
 185 constant depth channel is routed upstream for 100 km, to enable the tide wave to dissipate and  
 186 prevent reflection off an upstream boundary. The tidal amplitude to depth ratio ( $\frac{\xi}{h}$ ) is assumed  
 187 small, and river flow ( $Q_R$ ) is held constant (e.g., Kukulka and Jay, 2003a; Familkhalili et al., 2020).  
 188 Applying these assumptions and combining Eq. (1) and (2) yields the following differential  
 189 equation:

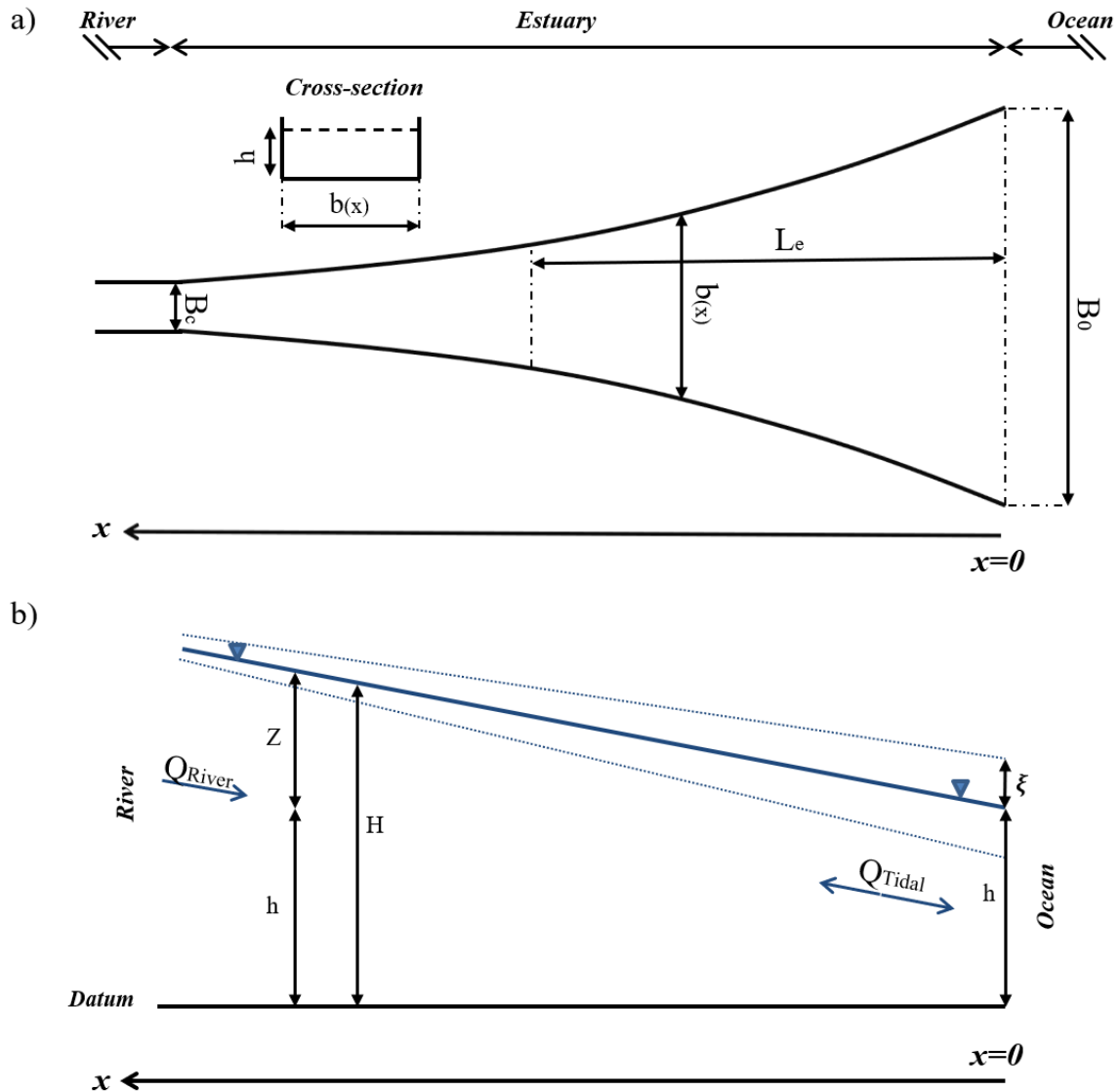
$$190 \quad \frac{\partial^2 Q_T}{\partial x^2} - \frac{1}{b} \frac{\partial b}{\partial x} \frac{\partial Q_T}{\partial x} - 2 \frac{1}{gh} U_R \frac{\partial^2 Q_T}{\partial x \partial t} + 2 \frac{1}{gh} U_R \frac{1}{A} \frac{\partial A}{\partial x} \frac{\partial Q_T}{\partial t} - \frac{1}{gh} \frac{\partial^2 Q_T}{\partial t^2} - \frac{b}{gh} \frac{\partial K}{\partial t} = 0 \quad (3)$$

191 We linearize the frictional term ( $K = C_d|u|u$ ) using Chebyshev polynomials (Dronkers, 1964) to  
 192 approximate the frictional term,  $u|u|$ . Following Godin (1991, 1999), only the first and third order  
 193 terms of the dimensionless velocity are retained, yielding:

$$194 \quad \frac{u|u|}{U_{(x)}^2} \approx Au' + Bu'^3 \quad (4)$$

195 where  $A = \frac{16}{15\pi}$ ,  $B = \frac{32}{15\pi}$ ,  $U_{(x)}$  is a function of  $x$  and is the maximum value of the total current  
 196 ( $U_R + U_T$ ), where  $U_R$  and  $U_T$  are maximum river and tidal velocity, respectively, and  $u'$  is a non-

197 dimensionalized velocity defined as  $\frac{u}{|U(x)|}$  (Doodson, 1956; Godin, 1991). See Familkhalili et al.,  
 198 (2020) for additional details.



199

200 Figure 1. (a) Idealized bathymetry and plan view of the conceptual model and (b) definition of the water surface  
 201 slope, modified from Kukulka and Jay (2003b). Along channel direction  $x$  is upstream with  $x=0$  at the ocean. The  
 202 convergent section of the model domain is 1.5 times the convergence length and the river channel at the left-hand  
 203 side extends an additional 100 km to enable tidal and surge constituents to damp out. See Appendix for a description  
 204 of parameters.

205 The sectionally and vertically averaged velocity term in Eq. (3) ( $u = Q/A$ ) is decomposed into three  
 206 sinusoidal wave components and a constant river discharge:

$$u = -u_r + \sum_{i=1}^3 u_i \cos(\omega_i t + \phi_i) \quad (5)$$

207 where  $u_r$  is the river flow velocity ( $m s^{-1}$ ), and  $u_i$ ,  $\omega_i$ ,  $\phi_i$  are velocity amplitudes, frequencies,  
 208 and phases, respectively. Although river discharge is not constant on seasonal or weather systems  
 209 (5-7 day) time scales, we assume for simplicity that the change over a tidal cycle or storm surge  
 210 wave (generally  $<2$  day time-scale) can be neglected. This limits our analysis to river systems with  
 211 a long-response time, i.e., our approach is inappropriate for short, steep, flashy systems with flood  
 212 time scales  $< 2$  days.

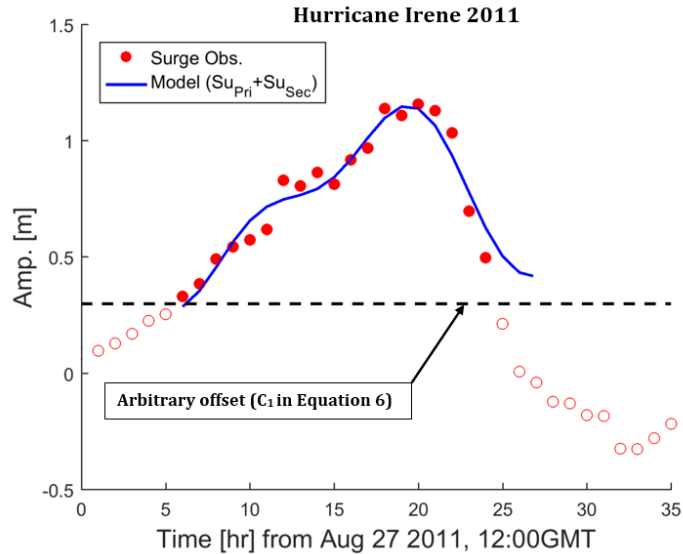
213 We use a multi-segment approach (Dronkers, 1964), to divide the model domain into  $N$  segments,  
 214 each has a constant depth and exponentially varying width. This approach produces a system of  
 215  $2N$  linear equations with  $2(N-1)$  internal, one seaward, and one landward boundary conditions. The  
 216 landward of our analytical model is forced by a no-reflection condition with constant discharge  
 217 and the seaward boundary (see Fig. 1) is forced by 3 sinusoidal water level signals. One of the sine  
 218 waves represents the main semidiurnal tidal constituent, and two of the sine waves represent the  
 219 elevated water level of the surge signal in terms of primary and secondary components, denoted  
 220 by the *Pri* and *Sec* subscripts (Famalkhalili et al., 2020):

$$Surge = \underbrace{A_{Pri} \cos(\omega_{Pri} t + \phi_{Pri})}_{Surge_{Pri}} + \underbrace{A_{Sec} \cos(\omega_{Sec} t + \phi_{Sec})}_{Surge_{Sec}} + \underbrace{C_1}_{Constant} \quad (6)$$

221 where  $A$  is the amplitude,  $\omega$  is the frequency,  $\phi$  is the phase, and  $C_1$  is an arbitrary offset. For  
 222 simplicity, the surge is treated as a free wave within the model domain, i.e., we neglect the effect  
 223 of wind stress and any locally generated component of surge.

224 An example fit using two sinusoidal waves to a surge caused by Hurricane Irene (August 2011) is  
 225 shown in Fig. 2. The surge signal is calculated by subtracting predicted tide from observed water  
 226 level at Lewes, DE (NOAA Station ID: 8557380). Fitting two sinusoidal waves approximates the  
 227 surge signal with correlation of  $R^2=0.95$  and root-mean-square-error of 0.05 m (Fig. 2). The fit is  
 228 valid for the time period that the surge remains above the dashed line.





229

230 Figure 2. An example of decomposing surge into two sinusoidal waves. The red circles represent surge and are  
 231 calculated by subtracting predicted tide from measured water level during Hurricane Irene (2011) at Lewes, DE  
 232 (NOAA Station ID: 8557380). The blue line is the model fit that is the sum of  $Su_{pri}$  and  $Su_{sec}$  and black dashed line  
 233 shows the threshold constant  $C_1$ , per Eq. (6).

234 Typical amplitudes, frequencies, and phases of the two component surge waves are determined by  
 235 fitting two sinusoids to 354 storm surge events from Lewes, DE. These results are used to define  
 236 the parameter space that we investigate (Sect. 4) and are typical of coastal storm surge  
 237 characteristics on the mid-Atlantic Bight. Only significant events, with surges larger than 0.5 m,  
 238 are fit. The largest resulting primary surge wave amplitude was about 1.1 m, larger than but of the  
 239 same order as the main tidal constituent ( $M_2 = 0.6$  m). The statistically significant fits ( $R^2 = 0.91$ )  
 240 have average primary and secondary surge periods of  $\sim 29$  and  $\sim 16$  h, respectively.

## 241 2-2- River discharge effects on water surface slope

242 The presence of river discharge ( $Q_R$ ) and tidal transport ( $Q_T$ ) causes stronger ebb currents ( $|Q_T| +$   
 243  $|Q_R|$ ) and weaker flood currents ( $|Q_T| - |Q_R|$ ). The resulting non-linear interaction and increased  
 244 friction typically reduces the tidal range, delays arrival of high and low water (e.g., Godin, 1985;  
 245 Hoitink and Jay, 2016), and generates tidal distortion (asymmetry), expressed as the presence of  
 246 overtides, e.g.,  $M_4$  in semidiurnal dominant systems (Parker, 1991). The increased friction also  
 247 influences subtidal water levels, producing a larger river slope (Kukulka and Jay, 2003b;  
 248 Buschman et al., 2009; Kästner et al., 2019). However, typical coastal plain systems in the western  
 249 Atlantic have low river flow relative to tidal transport. For example, the  $\sim 200 \text{ m}^3 \text{ s}^{-1}$  average annual  
 250 river discharge of the Saint Johns River Estuary, Florida, is about 5 % of total discharge (river +  
 251 tides) (Talke et al., 2021). Similarly, the Delaware River Estuary has mean and median river flows  
 252 at Trenton, NJ of  $\sim 340 \text{ m}^3 \text{ s}^{-1}$  and  $285 \text{ m}^3 \text{ s}^{-1}$ , respectively, small compared to tidal flow of  $\sim 23 \times 10^4$   
 253  $\text{m}^3 \text{ s}^{-1}$  at the mouth (USGS, 2018; Munchow et al., 1992). The Cape Fear River has an average

254 river discharge of  $268 \text{ m}^3 \text{ s}^{-1}$  (Familkhalili and Talke, 2016), which is less than 5 % of total  
 255 averaged ebb-tidal flow (Olsen, 2012).

256 River flow alters the water surface slope, and this behavior influences the spatial distribution of  
 257 total water level (e.g., Fig. 1b). Here, we use the tidally averaged one-dimensional equation of  
 258 motion to investigate water level gradients, following Kukulka and Jay (2003b) and Godin (1999).  
 259 For simplicity, the component of mean water level caused by the tidal Stokes drift is neglected.  
 260 The parameter  $h$  is the mean depth of water ( $m$ ),  $\xi$  is the tidal amplitude ( $m$ ) (small compared to  
 261 depth),  $Z$  is the perturbation in the water surface elevation due to river discharge  $Q_R$ , and is  
 262 assumed to be much smaller than  $h$ . In this study, normalized river flow velocity (applied at the  
 263 upstream boundary) is parameterized as the ratio of the river velocity magnitude to the magnitude  
 264 of the major tidal component velocity at the ocean boundary (i.e.,  $\frac{|u_r|}{|u_{D_2}|}$  or  $\theta$  hereafter). To evaluate  
 265 the effect of elevated river discharge, we consider a river flow ratio of 0 to 1. The ratio of  $\theta = 1$   
 266 represents a case in which river and tidal flows are comparable, and thus is outside the zone of our  
 267 assumptions; however, comparisons with numerical model results suggest that results below this  
 268 ratio are reasonable (see Sect. 3.1). Therefore, we assess both low-flow conditions and conditions  
 269 in which the river flow is comparable to tidal discharge.

270 Previous studies (e.g., Ralston et al., 2019; Helaire et al., 2019; Talke et al., 2021) showed that  
 271 reduced friction due to increased channel depth can alter the tidally averaged water level gradient  
 272 ( $\frac{\partial Z}{\partial x}$ , Fig. 1b). This water level gradient (river slope) can be determined from the one-dimensional  
 273 equation of motion (Godin, 1999):

$$\underbrace{\frac{1}{g} \frac{\partial \bar{u}}{\partial t}}_{\text{Local acceleration}} + \underbrace{\frac{\bar{u}}{g} \frac{\partial \bar{u}}{\partial x}}_{\text{Convective acceleration}} = - \underbrace{\frac{\partial H}{\partial x}}_{\text{Pressure gradient}} - \underbrace{\frac{\bar{u}|\bar{u}|}{C_h^2(h + \xi)}}_{\text{Friction}} \quad (7)$$

274 where  $\bar{u}$  is tidally averaged value of the current at  $x$  ( $ms^{-1}$ ),  $g$  is the acceleration due to gravity  
 275 ( $ms^{-2}$ ),  $C_h$  is Chézy coefficient ( $m^{1/2}s^{-1}$ ), and  $h$  is the mean depth of water ( $m$ ). Scaling the  
 276 terms in Eq. (7) using values typically found in estuaries (e.g., Godin and Martinez, 1994; Kukulka  
 277 and Jay, 2003b, Buschman et al., 2009) shows that zero-order balance is between the pressure  
 278 gradient and the friction term, so that the entire left-hand side of Eq. (7) can be neglected. We  
 279 adopt this simplification for our idealized geometry, but note that convective term may be locally  
 280 important in real systems with complex geometry (e.g., Helaire et al., 2019). The cross-sectional  
 281 area in our model varies smoothly (exponentially) over a large length scale; thus our approach  
 282 neglects convective effects in the mean momentum balance. We also neglect the riverbed slope,  
 283 which is typically small in estuaries, particularly in modern dredged systems (see e.g., Talke et al.,  
 284 2021). Within the upstream reaches of tidal rivers, the bed slope often increases and is important  
 285 dynamically (Kästner et al., 2019); therefore, we restrict our analysis and interpretation to estuarine

286 reaches. As before, we assume that the tidal amplitude to depth ratio ( $\frac{\xi}{h}$ ) is small. Given these  
 287 assumptions, we simplify Eq. (7) to the following balance (Godin and Martinez, 1994):

$$\frac{\partial \bar{H}}{\partial x} = -\frac{\bar{u}|\bar{u}|}{C_h^2 \bar{h}} \quad (8)$$

288 where  $\bar{H}$  is total water elevation and  $\bar{h}$  is the mean water level (the overbar denotes the tidally  
 289 averaged value). The low-frequency momentum Eq. (8) shows that the surface slope is defined by  
 290 the bed stress term. Using Eq. (4), we use a polynomial form of the bed stress ( $\bar{u}|\bar{u}|$ ) to solve Eq.  
 291 (8).

### 292 3- Model validation

293 The above tide-surge analytical model has previously been compared against two one-constituent  
 294 analytical models (the Toffolon and Savenije, 2011 and Jay, 1991 tidal solutions) and idealized  
 295 Delft-3D numerical model results for situations without river flow (Familkhalili et al., 2020).  
 296 Results showed that our analytical model is capable of capturing tidal wave amplitudes that are in  
 297 good agreement with numerical models results. In this section, we update the validation to include  
 298 the effects of river flow and compare our results against idealized Delft-3D numerical model  
 299 results using the same bathymetry and forcing (Type I). Then, we compare our analytical model  
 300 results against an idealized numerical model developed for the Cape Fear Estuary, North Carolina  
 301 (Familkhalili and Talke, 2016). This numerical model simulates storm surge from tropical storms  
 302 by using a parametric model of hurricane wind and pressure forcing that is applied over the  
 303 continental shelf (Type II). Table 1 shows the model parameters that were used to compare  
 304 analytical model results with numerical models.

305 Table 1. Analytical model parameters used in this study. See Appendix for a description of  
 306 parameters. Non-dimensional river discharge ( $\theta$ ) is applied at the upstream boundary and tide and surge  
 307 waves are applied at the ocean boundary (i.e., the estuary mouth,  $x=0$  in Fig 1).

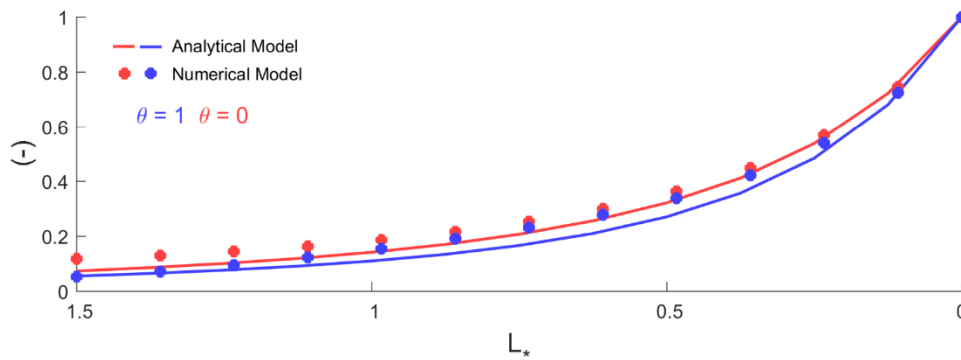
<i>Type</i>	$B_0$ (km)	$L$ (km)	$L_e$ (km)	$B_c$ (km)	$L_c$ (km)	$h$ (m)	$\theta$	<i>Tide</i> { Amp. (m) } { Period (h) }	<i>Surge</i> { Amp. (m) } { Period (h) }
I	5	120	80	1.1	100	5-7-10-15	0-0.25-0.5-1	{0.5} {12}	{0.5} {24} + {0.25} { 8 }
II	3	30	20	0.7	100	7-10-13-15	0	{0.5} {12}	{0.5} {12} + {0.25} { 6 }

308

309 **3-1- Idealized numerical models with similar forcing**

310 Analytical/numerical comparisons were made for a weakly convergent and strongly dissipative  
311 estuary with constant depth of 5m and a width profile defined by Type I (Table 1, see Fig. 1). The  
312 estuary section of the model domain ( $L$ ) is 120 km, 1.5 times the convergence length. Both  
313 analytical and numerical models are forced by the  $K_1$ ,  $M_2$ , and  $M_3$  tidal constituents at the ocean  
314 boundary, two of which ( $K_1$  and  $M_3$ ) combined represent a surge wave (Table 1). We further  
315 analyze the numerical model results by using harmonic analysis (e.g., Leffler and Jay, 2009).

316 Figure 3 shows the spatial pattern of the dominant tidal constituent ( $M_2$ ) amplitude normalized by  
317 its value at the estuary mouth. The analytical model results closely resemble the numerical model  
318 results with a root-mean-square error of 0.02 m for the three-wave model with and without river  
319 flow (blue and red colors in Fig. 3), showing that this idealized analytical model can properly  
320 estimate spatial variability of surge along an estuary.

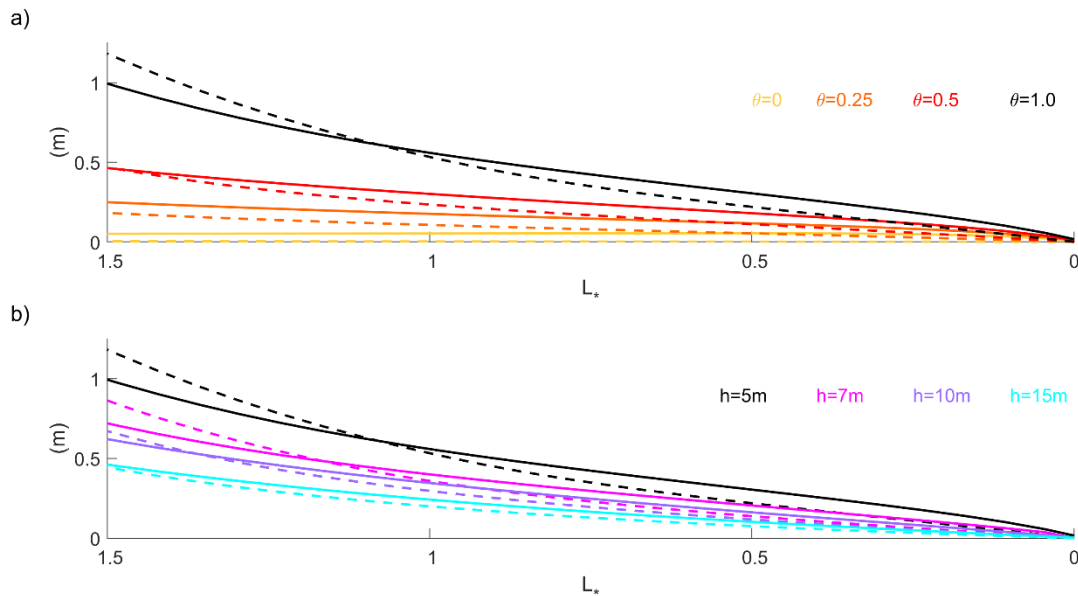


321  
322 Figure 3. Dominant tidal constituent ( $M_2$ ) amplitude in a 5 m deep estuary for three tides models ( $K_1$ ,  $M_2$ , and  $M_3$ )  
323 with and without river flow ( $\theta=0-1$ ). The  $x$  axis is the estuary length normalized by the convergence length scale  
324 ( $L_* = x/L_e$ ) and the vertical axis is normalized by  $M_2$  amplitude at the ocean boundary ( $L_*=0$ ).

325 In addition, results for the tidally averaged water levels (i.e.,  $Z$ ; see Fig. 1) under conditions with  
326 both tidal and river-flow forcing are consistent with numerical models, as shown in Fig. 4 for a  
327 weakly convergent estuary. The water level profiles vary with  $\theta$  (normalized flow velocity) for  
328 both the analytical model (dashed lines) and the numerical model (solid lines). In general, the  
329 analytical model slightly underestimates numerical results. The root-mean-square deviation  
330 between the numerical and analytical surface profiles are 0.03, 0.08, 0.09, and 0.10m for a  $\theta$  of 0,  
331 0.25, 0.5, and 1.0, respectively, or roughly 3-8 % of the total super-elevation above sea-level (Fig.  
332 4a). The pattern seen in Fig. 4 can be explained by Eq. (8), in which as river discharge increases  
333 (greater  $\theta$ ), the depth averaged velocity increases, and a larger water surface slope ( $\frac{\partial H}{\partial x}$ ) is needed  
334 to balance the Eq. (8).

335

336



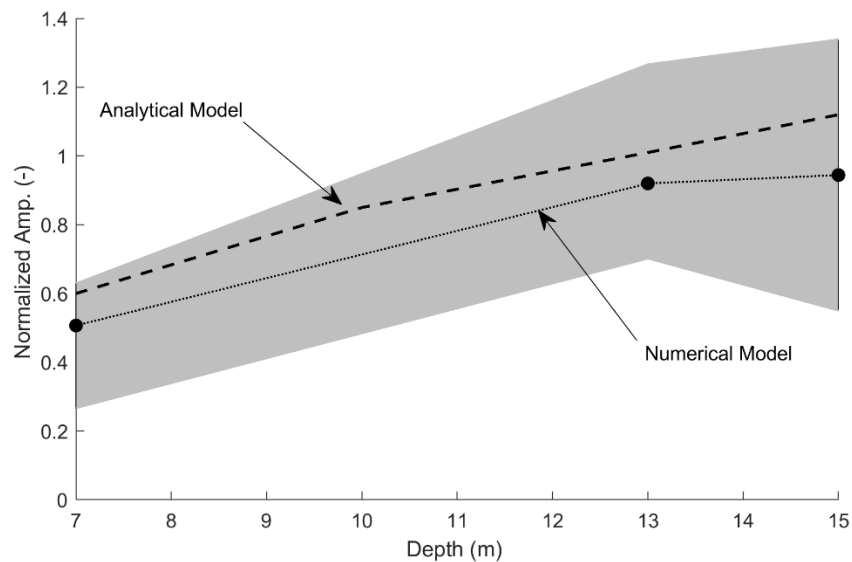
337

338 Figure 4. (a) The importance of river flow (i.e.,  $\theta$  at  $L_*=1.5$ ) for 5m depth and (b) the importance of channel depth  
339 for  $\theta=1$  in an idealized three waves model. The vertical axis is tidally averaged water level and horizontal axis  
340 represents dimensionless coordinate system of  $L_* = x/L_e$ . Solid and dashed lines represent numerical and analytical  
341 model results, respectively. The black solid and dashed lines represent same scenario ( $h=5$  m,  $\theta=1$ ) in both (a) and  
342 (b).

### 343 3-2- Idealized numerical model with parametric hurricane forcing

344 We further validate our analytical model results (Type II) with the idealized numerical modeling  
345 of Familkhalili and Talke (2016). This model includes a storm surge produced at the continental  
346 shelf and six semidiurnal and diurnal tidal constituents. Upstream of river kilometer 12, the estuary  
347 is convergent with an  $e$ -folding length scale of  $\sim 20$  km. The analytical model uses similar geometry  
348 (Table 1), uses the dominant tidal constituent ( $M_2$ ) at the estuary mouth and assumes that the  
349 primary surge wave has a period of 12 h. As in the numerical model, river flow is set to zero (Table  
350 1). We compare our analytical results at  $\sim L_* = 1.5$  with the corresponding location in the numerical  
351 model (Wilmington, North Carolina). For a shallow estuary of 7 m, the analytical model suggests  
352 that the storm surge wave is damped by  $\sim 40\%$  (from 0.5 m to 0.3 m) between the coast and  $L_* =$   
353 1.5 (Fig. 5). This damping is within the range of modeled results for a tropical storm surge at  
354 Wilmington ( $L_* \sim 1.5$ , Fig. 5). In a deeper configuration (mean depth = 15 m), the analytical model  
355 (this paper) finds a 12% increase in surge amplitude from the coast, well within the normalized  
356 amplitude of 0.55-1.35 found in Familkhalili and Talke (2016). Hence, both the sense of change  
357 as depth increases and the order of magnitude of change is consistent between the numerical and  
358 analytical model, improving our confidence in results (Fig. 5).

359



360

361 Figure 5. Comparison of normalized surge amplitude as a function of depth for an estuary resembling the Cape Fear  
 362 Estuary at an inland location at the approximate location of Wilmington, North Carolina. The dashed line is the  
 363 analytical model result, and the solid line is the numerical result. The idealized numerical model uses a surge event  
 364 with a mean amplitude of 0.6m at the ocean boundary (data from Familkhalili and Talke 2016). The fill area is the  
 365 range of results due to different relative phase of the storm surge and tide wave. The ‘Analytical model’ results are  
 366 for a 12 h surge that had an amplitude of 0.5 m and is evaluated at  $L_* = 1.5$ , at the approximately same location as  
 367 the numerical model. The y-axis is normalized surge amplitude and equals one at the ocean boundary.

368 The results of the model comparison (Fig. 3, 4 and 5) show that both the analytical and idealized  
 369 numerical models produce broadly consistent results. Therefore, our neglect of acceleration in the  
 370 subtidal model (Fig. 4) and the use of linearized friction is justified. Both numerical and analytical  
 371 models are complementary tools. A 3D model with resolved bathymetry is clearly best used to  
 372 evaluate the specific effect of bathymetric alterations in a particular estuary (e.g., Pareja-Roman  
 373 et al., 2020; Helaire et al., 2020), or to run simulations using complex, real valued boundary forcing  
 374 (river and coastal). But our analytical model runs substantially more quickly than even the  
 375 idealized numerical models, facilitating investigation of a larger parameter space. Moreover,  
 376 numerical models cannot unambiguously separate tide, fluvial, and surge effects. Currently, the  
 377 best-practice approach is to run the numerical model with and without relevant forcing; for  
 378 example, by running a surge model with and without tides, one can approximate the effect that  
 379 tides have on total water level (Shen et al. 2006). When combined, tide and surge wave travel  
 380 faster (due to deeper water depth; see Horsburgh and Wilson, 2007), and frictional energy loss in  
 381 each wave component is also larger (Familkhalili et al., 2020). Due to the multiple feedbacks and  
 382 nonlinear interactions, decomposing numerical results into individual surge and tide wave  
 383 transformations is inherently ambiguous. The analytical approach, while not including all  
 384 interactions (such as the phase modulation caused by depth variability), is able to individually  
 385 estimate transformations in the primary surge and tide constituent amplitudes, also under  
 386 conditions of different river discharge. This approach, to our knowledge, has not previously been

387 approached to understanding the fundamental bathymetric and boundary condition factors that  
 388 influence compound events.

#### 389 **4- Dimensional and non-dimensional parameter space studied**

390 We use our validated analytical model to further investigate the effects of channel depth, river  
 391 flow, channel width convergence, and surge time scale on the spatial evolution of water levels  
 392 along estuaries. For all simulations, the primary tidal constituent period and amplitude are fixed to  
 393 12 h (i.e., a semidiurnal or  $D_2$  wave) and 0.5 m, respectively, a value that is typical of the semi-  
 394 diurnal tide wave on the U.S. East Coast (Table 1). To study the effects of width convergence, we  
 395 test both weakly ( $L_e=80$  km) and strongly convergent ( $L_e=20$  km) conditions (see e.g., Jay, 1991;  
 396 Lanzoni and Seminara, 1998). Table 1 shows the parameter space used in the model. The primary  
 397 and secondary surge amplitudes are set to be 0.5 and 0.25 m, respectively (Eq. 6) and the estuary  
 398 mouth ( $B_0$ ) is assumed to have a width of 5 km. A sensitivity analysis is carried out by varying the  
 399 parameters in Table 1 individually, with other parameters held constant, resulting in a total of 128  
 400 parameter combinations (i.e., four different values for depths, four different values for river flow,  
 401 four different periods combination, and two convergence length scales).

402 Table 1: Parameter space used in analytical model

<i>Channel Depth (m)</i>	5, 7, 10, 15
<i>Su<sub>pri</sub> Amp. (m)</i>	0.5
<i>Su<sub>sec</sub> Amp. (m)</i>	0.25
$\left( \begin{array}{l} \text{Su}_{pri} \text{ Period (hr)} \\ \text{Su}_{sec} \text{ Period (hr)} \end{array} \right)$	$\left( \begin{array}{l} 12 \\ 6 \end{array} \right), \left( \begin{array}{l} 24 \\ 12 \end{array} \right), \left( \begin{array}{l} 48 \\ 24 \end{array} \right), \left( \begin{array}{l} 72 \\ 36 \end{array} \right)$
<i>D<sub>2</sub> Amp. (m)</i>	0.5, 1
<i>D<sub>2</sub> Period (h)</i>	12
<i>D<sub>1</sub> Amp. (m)</i>	0.5, 1
<i>D<sub>1</sub> Period (h)</i>	24
<i>Upriver flow velocity (<math>\theta = \frac{ u_r }{ u_{D_2} }</math>) at <math>L_* = 1.5</math></i>	0, 0.25, 0.5, 1
<i>Convergence length scale, <math>L_e</math> (km)</i>	80 (weakly convergent), 20 (strongly convergent)

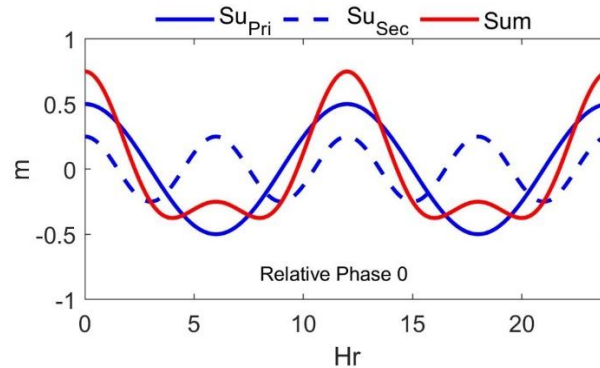
403

404 Non-dimensional variables provide insights into which parameters produce the most effect on  
 405 system response. From the scaling of Eq. (3) (see also Familkhalili et al., 2020), we derive the  
 406 three most relevant independent non-dimensional variables:

- 407 • Parameter ( $\Omega$ ) represents the ratio of  $Su_{Pri}$  period to  $D_2$  period and represents the  
 408 influence of primary surge wave period on tide-surge interactions.
- 409 • The friction number ( $\psi = \frac{C_d \xi \omega^2 L_e^3}{gh^3}$ ) shows the effects of changing surge wave  
 410 properties, which are influenced by depth ( $h$ ), surge frequency ( $\omega = \frac{1}{T}$ ), and  
 411 convergence length-scale ( $L_e$ ); all affect the damping or amplification of surge  
 412 waves.
- 413 • Parameter ( $\theta$ ) represents the ratio of upriver velocity (at  $L_*=1.5$ ) to the major tidal  
 414 component ( $D_2$ ) velocity at the estuary mouth.

415 For plotting purposes, we define two additional non-dimensional numbers:  $Su_{Pri}$  normalized  
 416 amplitude ( $A_* = \frac{Amp. Su_{Pri}}{Surge Amp. at Ocean Boundary}$ ) and a dimensionless coordinate system of  $L_* =$   
 417  $x/L_e$ , where  $L_*$  is normalized length.

418 In our models, we assume that the two surge waves are symmetric with a phase lag ( $\phi$  in Eq. (5))  
 419 of zero degrees between  $Su_{Pri}$  and  $Su_{Sec}$ , resulting in a repeating and symmetric storm surge wave  
 420 (see Fig. 6). This simulates a storm surge in which there is initially a draw-down in water level,  
 421 followed by the positive storm surge. To test the most frictional case, we also define the relative  
 422 phase lag between the  $D_2$  wave and surge to be zero.



423  
 424 Figure 6. A symmetric surge wave which is the result of two sinusoidal waves (i.e.,  $Surge = Su_{Pri} + Su_{Sec}$ ).

## 425 5- Results and discussion

426 We employ the validated model to study how bathymetry, river discharge, and surge characteristics  
 427 affect water floods in an idealized estuary. First, the effects of surge amplitude and period on water

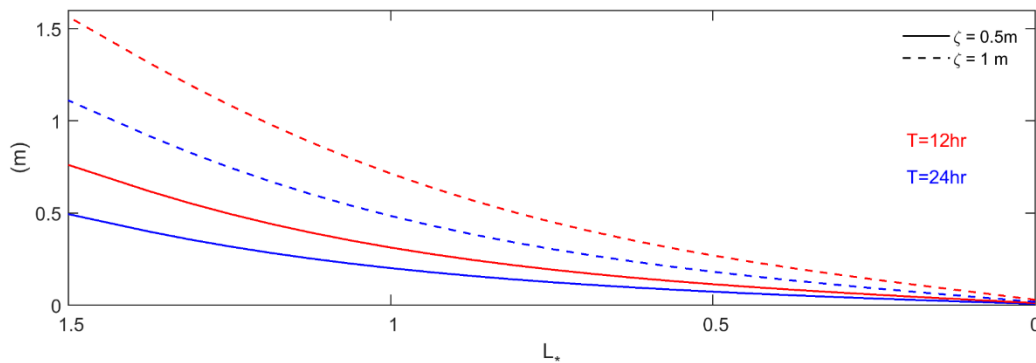


428 levels are examined. Then, the effects of river discharge and width convergence on surge amplitude  
 429 are presented, and finally compound flooding of tide, surge, and river flow is investigated.

### 430 5-1- Effects of wave characteristics on water level

431 The influence of wave characteristics (i.e., period and magnitude) on tidally averaged water level  
 432 is tested by modeling a set of waves with periods of 12 h and 24 h and amplitudes of 0.5 m and 1  
 433 m at the ocean boundary (i.e.,  $D_1$  and  $D_2$  in Table 1). Model results confirm, as suggested by the  
 434 friction number ( $\psi$ ), that increasing wave period ( $T = \frac{1}{\omega}$ ) or decreasing wave amplitude ( $\zeta$ ) has  
 435 similar effect as increasing depth ( $h$ ) and therefore would result in lower mean water levels (Fig.  
 436 7). Specifically, increasing wave period from 12 h (red lines) to 24 h (blue lines) reduces the mean  
 437 water level at  $L_* = 1.5$  from 0.75 m to 0.5 m, and from 1.56 m to 1.10 m for wave amplitudes of  
 438 0.5 m and 1 m at the ocean boundary ( $L_* = 0$ ), respectively. In other words, for the same boundary  
 439 amplitude, a shorter period wave produces larger mean water levels landward.

440



441

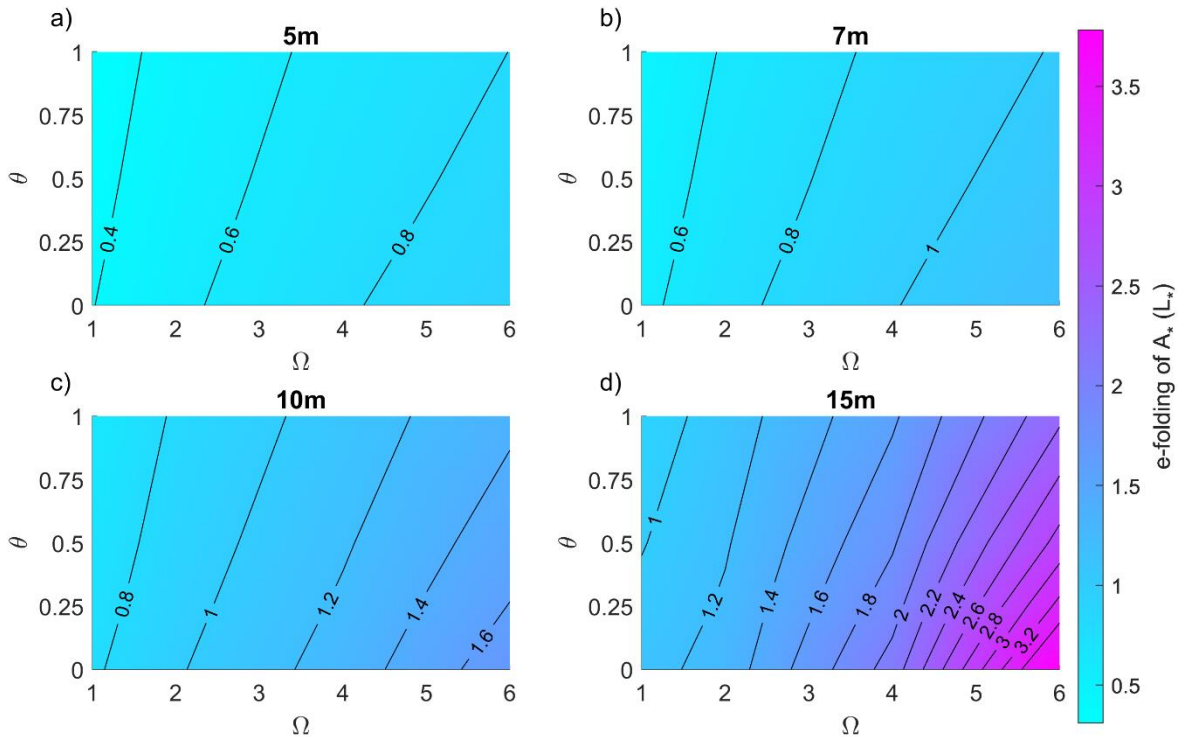
442 Figure 7. The effects of wave period (i.e., 12 h and 24 h) and amplitude (0.5 m and 1m at the ocean boundary  $L_* = 0$ )  
 443 on tidally averaged water level for 5 m depth channel in an idealized one sinusoidal wave model for  $\theta=1$ . Vertical  
 444 axis is tidally averaged water level, and the horizontal axis represents the estuary length normalized by the  
 445 convergence length scale (i.e.,  $L_* = x/L_e$ ).

### 446 5-2- Frictional effects of river discharge on surge amplitude

447 The rate at which a surge decays away from the ocean entrance varies with river flow and surge  
 448 period. Figure 8 shows the effects of river discharge and surge period on the  $e$ -folding length-scale  
 449 of  $Su_{pri}$  normalized amplitude ( $A_*$ ); the  $e$ -folding length is distance required for  $A_*$  to reach  $1/e \sim$   
 450 38% of boundary values. The longer the wave period, the more slowly surge normalized amplitude  
 451  $A_*$  decreases as the surge moves landward (keeping all other variables constant). For example, Fig.  
 452 8a shows that a 12 h ( $\Omega = 1$ ) surge amplitude reaches an  $e$ -folding reduction in amplitude at  $\sim 0.4L_*$   
 453 compared to  $\sim 0.9L_*$  for the 72 h ( $\Omega = 6$ ) surge. The lower rate of spatial decay of surge amplitude  
 454 for lower frequency surge waves is caused by their lower velocity and consequent smaller frictional  
 455 effects.

456 Model results also show that higher river discharge will increase the damping of surge amplitudes  
 457 (Fig. 8). When ( $\theta = 0$ ), river flow is zero and only tide-surge nonlinear interactions can occur.  
 458 Hence, surge amplitudes decay more slowly for  $\theta = 0$  than for  $\theta > 0$  (compare the  $\theta = 0$  and  $\theta =$   
 459  $1$  cases in Fig. 8). The slanted contour lines highlight the effects of river flow; as  $\theta$  increases, the  
 460  $e$ -folding length-scale of normalized amplitude ( $A_*$ ) reduces for all surge periods ( $\Omega=1-6$ ) (Fig.  
 461 8a-d). Adding river flow to a surge with a primary period of 12 h ( $\Omega = 1$ ) reduces the  $e$ -folding  
 462 scale of damping from  $0.4L_*$  ( $\theta = 0$ ) to  $0.34L_*$  ( $\theta = 1$ ), for the 5 m depth case ( $\sim 15\%$  decrease;  
 463 Fig. 8a). The percent decrease in the  $e$ -folding scale is larger in a deeper, 15m channel, and  
 464 decreases from  $1.15L_*$  to  $0.95L_*$  ( $\sim 18\%$  decrease; Fig. 8d).

465 Surge amplitudes also decay more slowly (larger  $e$ -folding) in a deeper channel for all surge  
 466 periods (Fig. 8). Thus, the largest difference in normalized amplitude between a 12 h ( $\Omega = 1$ ) and  
 467 72 h ( $\Omega = 6$ ) surge occurs at larger depth ( $h=15$  m) with changes of  $\sim 1L_*$  to  $3.5L_*$  in the  $e$ -folding  
 468 length-scale of damping (Fig. 8d). Increasing the river discharge relative to the  $M_2$  velocity (larger  
 469  $\theta$ ) reduces the amplification of the surge wave and therefore the  $e$ -folding length scale of  
 470  $A_*$  reduces from  $\sim 3.5L_*$  to  $\sim 2.4L_*$  for  $Su_{Pri}$  of 72 h (Fig. 8d).



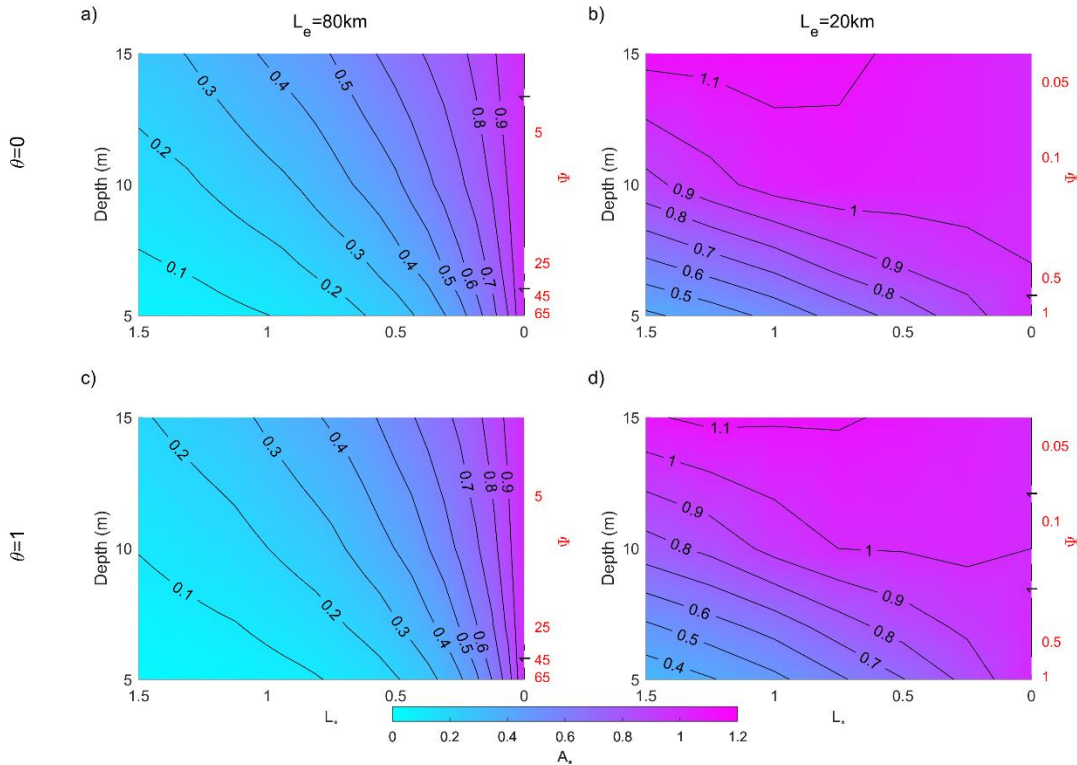
472 Figure 8. The effects of river flow ( $\theta = \frac{|u_r|}{|u_{D2}|}$ ) and surge periods ( $\Omega = \frac{Supri\ Period}{D_2\ Period}$ ) along an idealized weakly  
473 convergent estuary for channel depth of (a) 5 m, (b) 7 m, (c) 10 m, and (d) 15 m. The color scaling represents the  $e$ -  
474 folding length-scale of primary surge normalized amplitude ( $A_*$ ).

475 Consistent with other studies (e.g., Kukulka and Jay, 2003b; Hoitink and Jay, 2016), both the  
476 analytically and numerically modeled water level slope ( $\frac{dZ}{dL_*}$ ) is largest upstream and becomes  
477 significantly less near the coast. This is caused by the decreased river velocity (and friction)  
478 associated with the downstream increase in cross-sectional area. Therefore, we expect that varying  
479 the forcing or the geometry will impact mean water levels upstream, as river velocity magnitudes  
480 shift.

### 481 **5-3- Effects of width convergence on surge amplitude**

482 Long-wave propagation along an estuary is characterized by a balance of inertial effects, friction,  
483 and convergence. Figure 9 shows the normalized amplitude ( $A_*$ ) of the primary surge wave for  
484 weakly convergent (left panel, 9a and 9c) and strongly convergent estuaries (right panel, 9b and  
485 9d), for a 12 h surge period ( $\Omega = 1$ ). The contours represent the  $e$ -folding length-scale of primary  
486 surge normalized amplitude and the  $x$ -axis represents the dimensionless coordinate system of  $L_* =$   
487  $x/L_e$ . The factor 4X change in convergence length scale from 80 km (Fig. 9a, 9c) to 20 km (Fig.  
488 9b, 9d) alters the friction scale ( $\psi$ ) by a factor of 64.

489 The convergence of an estuary influences surge amplitudes (Fig. 9), similar to its well-known  
490 effects on tidal amplitudes (e.g., Jay, 1991). All surge amplitudes decrease landward for all depth  
491 cases in a weakly convergent ( $L_e=80$  km) estuary; effectively, convergence effects are much  
492 smaller than the bed friction and gravity effects and therefore long-wave amplitudes decrease (Fig.  
493 9a and 9c). Under strongly convergent conditions with no river flow, the primary surge amplitude  
494 decays less quickly in a deeper channel as it moves upstream than under weakly convergent  
495 condition (see Fig. 9a, b), and can even increase in the inland direction (see Fig. 9b). By contrast,  
496 increased river discharge produces greater damping in the surge wave (compare Fig. 9a and 9c, or  
497 Fig. 9b and 9d). For example, for friction factor of  $\psi = 0.5$  ( $h = 6.5$  m) and a location of  $L_* = 1$ ,  
498 the surge wave has damped to 60 % of its boundary value when the tidal to river flow ratio is  $\theta=1$   
499 (Fig. 9d) but is at 70 % of its boundary value when there is no river discharge (Fig. 9b). Hence,  
500 increasing river flow and decreasing channel depth both cause larger damping in the surge wave.

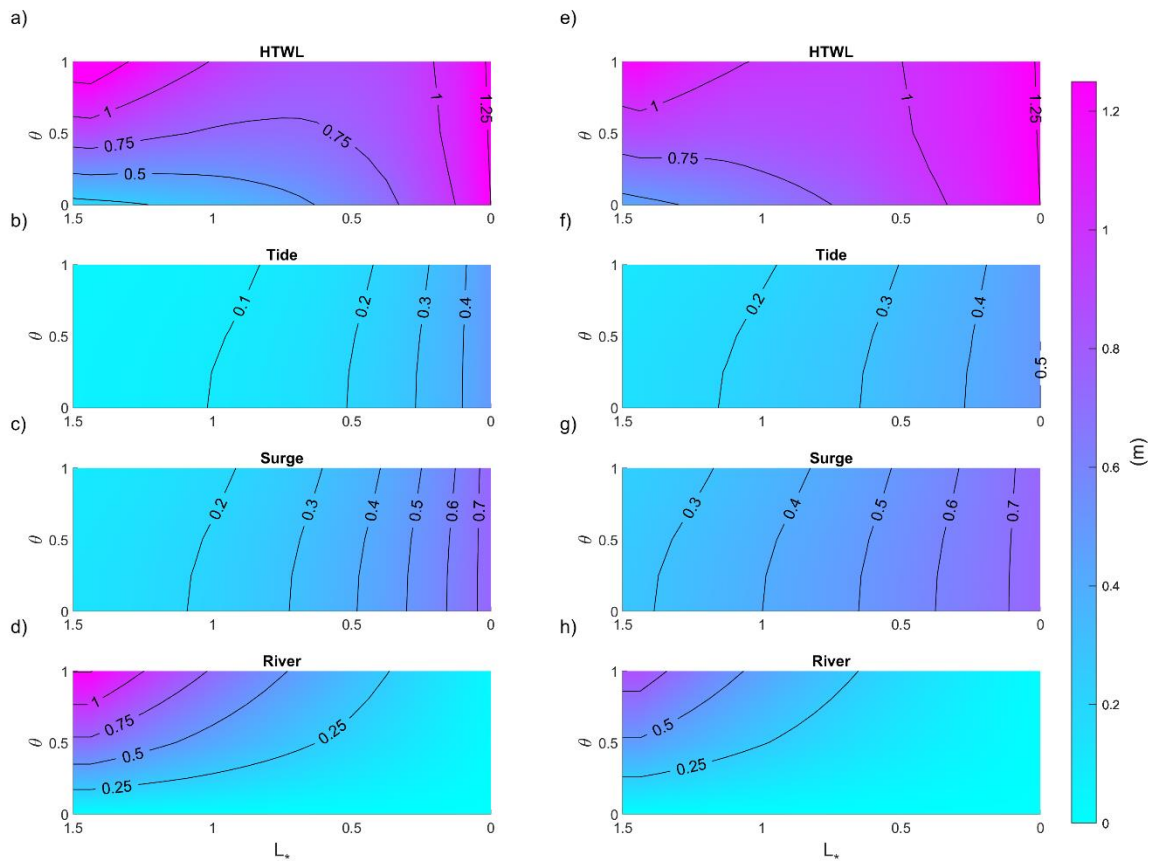


501

502 Figure 9. The effects of convergence length scale and river discharge on primary surge (12 h,  $\Omega = 1$ ) amplitude ( $A_*$  is  
 503 normalized amplitude) along a weakly convergent estuary,  $L_e = 80$  km (subplots a, c) and strongly convergent  
 504 estuary,  $L_e = 20$  km (subplots b, d). Left hand side vertical axis is channel depth and right-hand side vertical axis is  
 505 the corresponding non-dimensional friction number ( $\psi = \frac{C_d \xi \omega^2 L_e^3}{gh^3}$ ) and horizontal axis represents dimensionless  
 506 coordinate system of  $L_* = x/L_e$ .

#### 507 **5-4- Combined effects of tide, surge, and river flow on total water levels**

508 We next investigate how variations in river flow influence the Total Water Level (TWL), caused  
 509 by the combination of tide, storm surge, and river discharge effects. The highest possible total  
 510 water level (HTWL) during such a compound event occurs when the surge occurs at high water,  
 511 coincident with peak river flow. Because the timing of a meteorological event is usually random  
 512 relative to tides, and because peak surge usually precedes peak river discharge, HTWL rarely if  
 513 ever occurs. However, it is a useful metric of the potential flooding. Such a worst-case scenario  
 514 could occur, for example, when multiple storms occur in close succession. The HTWL therefore  
 515 provides a way to compare different parameter regimes and evaluate the effect of long-term  
 516 changes in the geometry of an individual estuary.



518

519 Figure 10. Combined contribution of tide, surge, and river flow to water level for depths of 5 m (left panel subplots)  
 520 and 10 m (right panel subplots). Colors and the labeled contours denote water level. The total water level (a and e) is  
 521 the combination of tidal amplitude (b and f), surge amplitude (c and g) and water level from river discharge (d and  
 522 h). The period of the primary surge ( $Su_{pri}$ ) is 24 h, the convergence length scale is 80km, the  $x$ -axis represents  
 523 dimensionless coordinate system of  $L_* = x/L_e$  (origin at estuary mouth, on right-hand side) and the  $y$ -axis shows the  
 524 non-dimensional river flow ( $\theta = \frac{|u_r|}{|u_{D2}|}$ ).

525 The HTWL (Fig. 10a and 10e) follows a pattern set by the contradictory effects of river flow and  
 526 marine forcing (tides and surge). Far upstream ( $L_* = 1.5$ ), river water levels are the largest factor,  
 527 particularly for larger  $\theta$ , but decay in the downstream direction (Fig. 10d and 10h). The surge and  
 528 tidal components of water level (e.g., Fig. 10b, 10c) decay in the opposite direction, from the  
 529 oceanic boundary towards the upstream boundary. For larger river flows ( $\sim \theta > 0.5$ ), the  
 530 counteracting factors produce a minimum HTWL in the middle part of the domain ( $L_* = 0.5-1.0$ ).  
 531 For small river flows, water levels monotonically decrease in the upstream direction.

532 Importantly, the HTWL is not merely the superposition of river flow, tide, and surge effects,  
 533 considered in isolation. Rather, as shown by the non-vertical contour lines for tides and surge (e.g.,  
 534 Fig. 10f and 10g), increases in the relative influence of river flow (larger  $\theta$ ) tend to reduce the  
 535 magnitude of tides and surge (see also Helaire et al., 2020). By contrast, increases in long-wave

536 magnitudes (tides, surge) at the ocean boundary increase the tidally averaged water level profile,  
537 as already established (Fig. 7; see also Buschman et al., 2009 and Talke et al., 2021).  
538 Simultaneously, long-wave magnitudes decrease more quickly, the larger they are at the ocean  
539 boundary (see also Familkhalili et al., 2020). Effectively, each component of water level influences  
540 the other, and itself: for example, tides within the domain depend on self-interaction (e.g., the  
541 boundary magnitude matters), and also on tide-surge and tide-river interaction. While the overall  
542 influence in terms of magnitude is relatively minor for the parameter space in Fig. 10, these  
543 observations show that non-linear tide-surge-river interactions during a compound event cannot  
544 be neglected. In particular, interactions would be larger in macrotidal systems, and/or for larger  
545 surges.

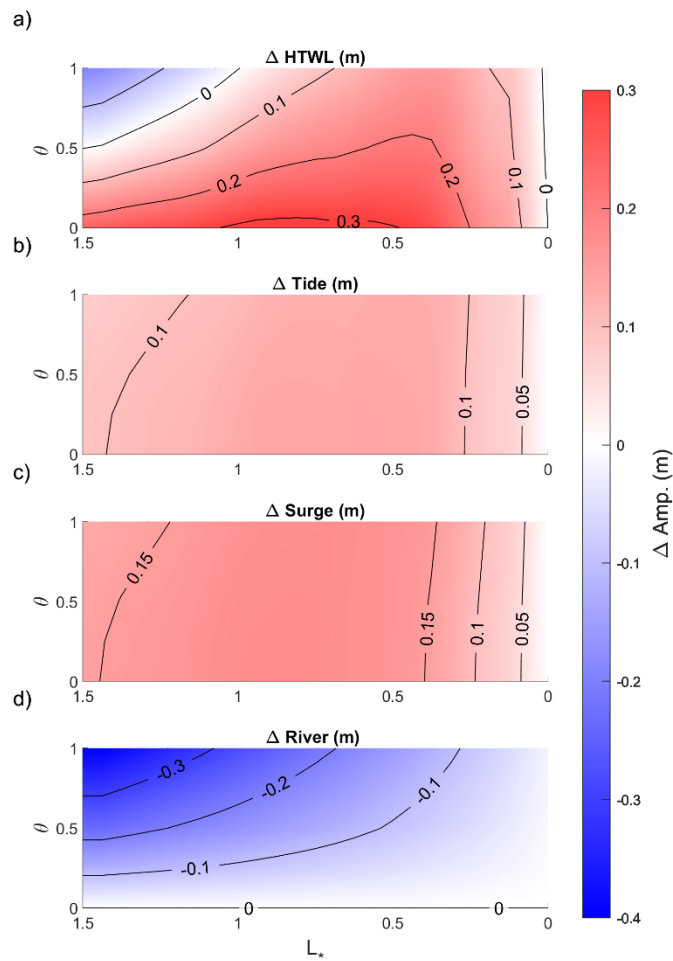
546 Changes in the depth of an estuary, whether by dredging, sea-level rise, or sedimentation/erosion,  
547 also exert a strong, spatially variable influence on the HTWL (Fig. 10 and 11). When depth is  
548 small (5m; Fig. 10a), the HTWL is greater in the upstream domain ( $L_* = 1.5$  and  $\theta > 0.5$ ) than in a  
549 larger depth case (10m; Fig. 10e). This occurs because a larger average river slope is needed to  
550 push the same amount of water seaward when depth is small, as suggested by Eq. (8) (see also  
551 Talke et al., 2021). However, smaller depths also lead to greater dissipation and frictional effects  
552 in the tide and surge wave, due to the same reduction in hydraulic drag (compare right-hand and  
553 left-hand side of Fig. 10, and their difference (Fig. 11)). Hence, tide and surge amplitudes increase  
554 when depth is increased, for all river discharges ( $\theta = 0-1$ ; Fig. 11b, c). The percent increase is less  
555 for higher river discharge; this is evident from the rightward slant of contours in Fig. 11b and 11c.  
556 Further, both tides and surge show a region of maximum change, located in mid-estuary (between  
557  $L_* = 0.5$  to 1; Fig. 11). Near the ocean boundary, changes are relatively small, also in percentage  
558 terms. Far upstream, the percent change in tidal range may still be significant, but the magnitudes  
559 themselves are small (see also Talke et al., 2021).

560 The differences in the response of river flow and storm surge to a depth increase lead to a *crossover*  
561 *point*, which we define as the location in which river flow effects on HTWL are larger than marine  
562 effects, for a given set of forcing conditions (see the zero-contour line in Fig. 11a). Since the  
563 crossover point moves upstream as depth increases (Fig. 12), processes such as dredging, erosion,  
564 or sea-level rise that increase depth can alter the relative influence of marine and river effects, for  
565 a given storm surge and river flow. Similarly, a decrease in mean river inflow, as has occurred in  
566 many river-estuaries due to flow regulation, may also cause a landward migration in the crossover  
567 point (Fig. 12).

568 Other factors that influence long-wave amplitudes also influence the crossover point, including the  
569 period of the surge (Fig. 8), convergence length  $L_e$  (Fig. 9), the boundary amplitude, and the  
570 relative phasing of tides and surge (see Familkhalili et al., 2020). The influence of many of these  
571 factors is explained by considering the non-dimensional friction number ( $\psi = \frac{c_d \xi \omega^2 L_e^3}{gh^3}$ ) (see Sect.  
572 2.1). This number suggests that increases in channel depth ( $h$ ) and wave period ( $T = \frac{1}{\omega}$ ) and

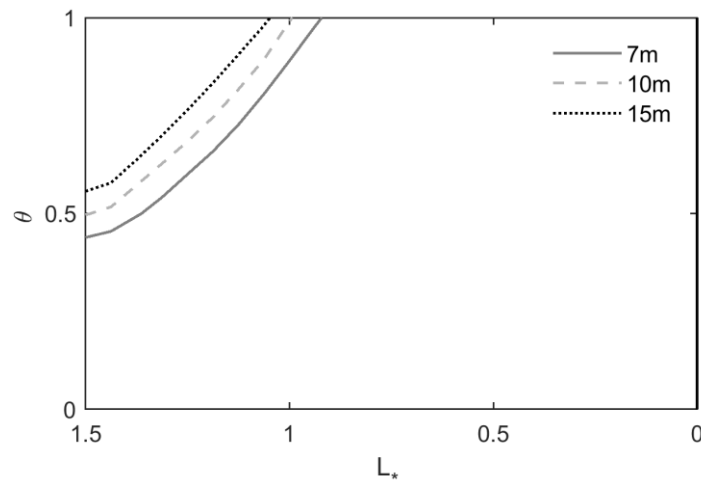
573 decreases in length scale ( $L_e$ ) have similar effects on wave amplitudes. For example, increasing  
 574 the depth from 5 m ( $\psi = 69$ ) to 15 m ( $\psi = 2.6$ ) causes  $A_*$  (i.e., normalized amplitude by ocean  
 575 boundary amplitude) to increase from  $\sim 0.06$  to 0.26 (Fig. 9a). Similarly, changing the surge period  
 576 from 12 to 60 h ( $\psi = 69$  to 2.8) changes  $A_*$  from  $\sim 0.06$  to 0.22 for a 5 m channel depth.

577 Other studies, such as Bilskie and Hagen (2018), have defined flood zone transitions between  
 578 marine and fluvial dominance; close to coast, tide and surge-based flooding dominates, while river  
 579 floods dominate far upstream. In between, there is a transition zone with compound flooding in  
 580 which both coastal and fluvial processes are important. Here, our model also suggests that the  
 581 transition zone location is sensitive to changes in estuary geometry, such as depth, in addition to  
 582 being dependent on the relative strength of river flow, tide, and surge amplitudes.



583  
 584 Figure 11. Comparison of contribution of tide, surge, and river flow to compound flooding between 5 m and 10 m  
 585 depth channel and  $S_{uPri} = 24$  h.  $\Delta$  represents the amplitude difference of each factor (HTWL, tide, surge, and river

586 flow) between two controlling depths. The convergence length scale is 80 km and  $x$ -axis represents dimensionless  
 587 coordinate system of  $L_* = x/L_e$  and  $y$ -axis shows non-dimensional river flow ( $\theta = \frac{|u_r|}{|u_{D2}|}$ ).



588  
 589 Figure 12. Crossover point location for 7-15 m channel depth compared to 5m case, ( $Su_{pri} = 24$  h and  $L_e = 80$  km).  $x$ -  
 590 axis represents dimensionless coordinate system of  $L_* = x/L_e$  and  $y$ -axis shows non-dimensional river flow ( $\theta =$   
 591  $\frac{|u_r|}{|u_{D2}|}$ ).

## 592 6- Conclusion

593 In this study, we have applied a new river-tide-surge analytical model to investigate the  
 594 interactions of tide, surge, and river flow along idealized estuaries. The novelty of our approach is  
 595 that we develop a quasi-linear analytical model, previously applied to tides, that considers the non-  
 596 linear interaction between tides, storm surge, and river discharge. To the best of our knowledge,  
 597 these processes (river flow + surge + tides) have not been explored within an analytical framework.  
 598 The model also elucidates the trade-offs caused by channel deepening, which can reduce mean  
 599 water levels but increase storm surge and tides.

600 We show that the rate of damping in a storm tide (surge + tide) is sensitive to fluctuations of river  
 601 discharge (Fig. 8), alterations in the surge period (Fig. 8), and channel geometry changes (width  
 602 convergence and depth) (Fig. 9). Model results show that the crossover point, which is the location  
 603 at which the river flow effects are larger than marine effects, moves upstream as channel depth  
 604 increases or as river flow decreases (Fig. 12). Thus, the spatial variability in compound flood risk  
 605 contributors (i.e., tide, surge, and river flow) change when an estuary is modified, or river  
 606 discharge changes. Generally, increasing the surge period has a similar effect as increasing the  
 607 depth; however, we note that our model is slightly more sensitive to depth, due to the cubic  
 608 relationship in the friction term, rather than the squared effect of period. The non-dimensional  
 609 friction number ( $\psi$ ) suggest that the effects of surge amplitude at boundary ( $\xi$ ) and drag coefficient  
 610 ( $C_d$ ) have a lesser, but still important, influence on the spatial damping of surge as the depth. We



611 conclude that in a shallow estuary the effects of friction are dominant over the convergence and  
 612 cause the wave amplitudes (tides and surge) to decrease, while deepening the estuary may cause  
 613 amplification of long-waves upriver of an estuary. As shown in Fig. 9, the amplification in storm  
 614 surge is particularly acute when the estuary is highly convergent.

615 Globally, natural and local anthropogenic changes in estuaries (e.g., sea-level rise, channel  
 616 deepening for navigation and landfilling) produce alterations in tidal and surge amplitudes (see  
 617 review by Talke and Jay, 2020, and references therein). This study shows that river flow and its  
 618 interaction with tides and surge must also be considered when evaluating changes to water levels.  
 619 For example, increasing the river discharge relative to tide velocity reduces the amplification of  
 620 the surge wave. Moreover, channel deepening produces a reduction in the water level caused by  
 621 river discharge, leading to a domain in which channel deepening produces lower water levels  
 622 upstream but larger water levels in the estuary (Fig. 10-12; see also Helaire et al, 2019 and Ralston  
 623 et al., 2019). Our findings are consistent with other studies that find that reduced frictional effects  
 624 (e.g., caused by channel deepening) can cause increases to tides and surge (see e.g., Ralston et al.,  
 625 2019; Talke et al., 2021). Overall, anthropogenic changes to estuary geometry and frictional  
 626 characteristics can cause large changes in the amplitude and spatial distribution of compound  
 627 flooding.

## 628 7- Appendix

629 This glossary provides definitions of the terms used in this manuscript.

Name	Definition	Unit
$A$	Channel cross-sectional area	$m^2$
$A_*$	Ratio of primary surge amplitude within the estuary to the surge wave amplitude at ocean boundary	-
$b$	Channel width	$m$
$B_0$	Estuary mouth width	$m$
$B_c$	River width	$m$
$C_d$	Drag coefficient	-
$D_1$	Diurnal tidal constituent	-
$D_2$	Semidiurnal tidal constituent	-
$g$	Gravitational acceleration	$m s^{-2}$
$h$	Channel depth	$m$
$K$	Bed stress divided by water density	$m^2 s^{-2}$
$L$	Length of estuary	$m$
$L_e$	Convergence length scale of estuary width	$m$
$L_c$	Constant width river channel length	$m$
$L_*$	Normalized length	-
$Q$	Cross-sectionally integrated flow	$m^3 s^{-1}$
$Q_R$	River flow discharge	$m^3 s^{-1}$

$Q_T$	Tidal transport	$m^3s^{-1}$
$Su_{pri}$	Primary surge wave	-
$Su_{sec}$	Secondary surge wave	-
$t$	Time	$s$
$T$	Surge period	$s$
$u_R$	River flow velocity	$ms^{-1}$
$u_T$	Tidal velocity	$ms^{-1}$
$U_R$	Maximum river flow velocity	$ms^{-1}$
$U_T$	Maximum tidal velocity	$ms^{-1}$
$x$	Along channel distance. Estuary mouth is at $x = 0$ and $x$ increases landward	$m$
$\xi$	Tidal amplitude	$m$
$\theta$	River velocity magnitude to the magnitude of the major tidal component velocity at the ocean boundary	-
$\rho$	Water density	$Kg m^3$
$\phi$	Wave phase	$rad$
$\omega$	Wave frequency	$s^{-1}$
$\Omega$	Ratio of primary surge period to main tidal component period	-
$\psi$	Friction number	-

630

## 631 **8- Author contribution**

632 Ramin Familkhalili: Methodology, Software, Validation, Formal analysis, Investigation, Data  
633 Curation, Writing - Original Draft, Writing - Review & Editing, Visualization

634 Stefan Talke: Conceptualization, Methodology, Formal Analysis, Resources, Writing - Review &  
635 Editing, Supervision, Project administration, Funding acquisition.

636 David Jay: Conceptualization, Methodology, Formal Analysis, Resources, Writing - Review &  
637 Editing, Supervision.

## 638 **9- Competing interests**

639 The authors declare that they have no conflict of interest.

## 640 **10- Data availability**

641 The data used are listed within the body of the manuscript and references.

642

## 11- Acknowledgements

643 Funding was provided by the US Army Corps of Engineers (award W1927N-14-2-0015) and the  
644 National Science Foundation (awards 1455350 and 1854946).

645

## 12- References

- 646 Bertin, X., Bruneau, N., Breilh, J. F., Fortunato, A. B., and Karpytchev, M.: Importance of wave  
647 age and resonance in storm surges: The case Xynthia, Bay of Biscay, *Ocean Modell.*,42,16–  
648 30, doi:10.1016/j. ocemod.2011.11.001, 2012.
- 649 Bilskie, M. V. and Hagen, S. C.: Defining Flood Zone Transitions in Low-Gradient Coastal  
650 Regions, *Geophys. Res. Lett.*, 45, 2761–2770, <https://doi.org/10.1002/2018GL077524>,  
651 2018.
- 652 Brandon, C.M., Woodruff, J.D., Donnelly, J.P., and Sullivan, R.M.: How unique was Hurricane  
653 Sandy? Sedimentary reconstructions of extreme flooding from New York Harbor. *Scientific*  
654 *Reports*, <http://dx.doi.org/10.1038/srep07366>, 2014.
- 655 Buschman, F. A., Hoitink, A. J. F., Van Der Vegt, M., and Hoekstra, P.: Subtidal water level  
656 variation controlled by river flow and tides. *Water Resources Research*, 45, W10420.  
657 <https://doi.org/10.1029/2009WR008167>, 2009.
- 658 Cai, H., Savenije, H. H. G., and Toffolon, M.: Linking the river to the estuary: influence of river  
659 discharge on tidal damping, *Hydrol. Earth Syst. Sci.*, 18, 287–304,  
660 <https://doi.org/10.5194/hess-18-287-2014>, 2014.
- 661 Chernetsky A. S., Schuttelaars, H. M., Talke, S. A.: The effect of tidal asymmetry and temporal  
662 settling lag on sediment trapping in tidal estuaries. *Ocean Dyn.* 60:1219–41, 2010.
- 663 Doodson A. T.: Tides and storm surge in a long uniform gulf. *Proceedings of the Royal Society of*  
664 *London*, A237, 325-343, 1956.
- 665 Dronkers, J. J.: *Tidal Computations in Rivers and Coastal Waters*, North-Holland, New York, 296–  
666 304, 1964.
- 667 Ensing H, de Swart H. E., Schuttelaars H. M.: Sensitivity of tidal motion in well-mixed estuaries  
668 to cross-sectional shape, deepening, and sea level rise: an analytical study. *Ocean Dyn.*  
669 65:933–50, <https://doi.org/10.1007/s10236-015-0844-8>, 2015.
- 670 Familkhalili, R., and Talke, S. A.: The effect of channel deepening on tides and storm surge: A  
671 case study of Wilmington, NC, *Geophys. Res. Lett.*, 43, 9138– 9147,  
672 doi:10.1002/2016GL069494, 2016.
- 673 Familkhalili, R., Talke, S. A., & Jay, D. A.: Tide-storm surge interactions in highly altered  
674 estuaries: How channel deepening increases surge vulnerability. *Journal of Geophysical*  
675 *Research: Oceans*, 125, e2019JC015286. <https://doi.org/10.1029/2019JC015286>, 2020.
- 676 Friedrichs, C. T., and Aubrey, D. G.: Tidal propagation in strongly convergent channels. *Journal*  
677 *of Geophysical Research*, 99(C2), 3321–3336. <http://doi.org/10.1029/93JC03219>, 1994.
- 678 Giese, B. S., and Jay, D. A.: Modeling tidal energetics of the Columbia River estuary, *Estuarine*  
679 *Coastal Shelf Sci.*, 29(6), 549–571, doi:10.1016/02727714(89)90010-3, 1989.
- 680 Godin, G.: Modification of rivertides by the discharge, *J. Waterway, Port, Coastal, Ocean Eng.*,  
681 1985, 111(2): 257-274, 1985.
- 682 Godin, G.: Compact approximations to the bottom friction term for the study of tides propagating  
683 in channels. *Continental Shelf Research* 11 (7), 579–589, 1991.

684 Godin, G.: The propagation of tides up rivers with special considerations on the upper Saint  
685 Lawrence River, *Estuarine, Coastal and Shelf Science*, 48, 307 – 324, 1999.

686 Godin, G., Martinez, A.: Numerical experiments to investigate the effects of quadratic friction on  
687 the propagation of tides in a channel, *Continental Shelf Research*, Vol. 14, No. 7/8, pp. 723-  
688 748, 1994.

689 Helaire, L. T., Talke, S. A., Jay, D. A., & Chang, H.: Present and Future Flood Hazard in the Lower  
690 Columbia River Estuary: Changing Flood Hazards in the Portland-Vancouver Metropolitan  
691 Area. *Journal of Geophysical Research: Oceans*, <https://doi.org/10.1029/2019JC015928>,  
692 2020.

693 Helaire, L. T., Talke, S. A., Jay, D. A., & Mahedy, D.: Historical changes in Lower Columbia  
694 River and estuary floods: A numerical study. *Journal of Geophysical Research: Oceans*, 124,  
695 7926–7946. <https://doi.org/10.1029/2019JC015055>, 2019.

696 Hoitink, A. J. F., and Jay, D. A.: Tidal river dynamics: Implications for deltas, *Rev. Geophys.*, 54,  
697 240–272, doi:10.1002/2015RG000507, 2016.

698 Horrevoets, A. C., Savenije, H. H. G., Schuurman, J. N., Graas, S.: The influence of river discharge  
699 on tidal damping in alluvial estuaries, *J. Hydrol.*, 294(4), 213–228, 2004.

700 Horsburgh, K. J., and Wilson, C.: Tide-surge interaction and its role in the distribution of surge  
701 residuals in the North Sea, *J. Geophys. Res.*, 112, C08003, doi:10.1029/2006JC004033,  
702 2007.

703 Jay, D. A.: Green's law revisited: Tidal long-wave propagation in channels with strong  
704 topography. *Journal of Geophysical Research*, 96(C11), 20585.  
705 <http://doi.org/10.1029/91JC01633>, 1991.

706 Jay, D. A., Devlin, A., Idier, D., Prococki, E., and Flick, E. R.: Tides and Geomorphology: Time  
707 Scales and Non-Stationary Processes, *Coastal and Submarine Geomorphology*, *Treatise on*  
708 *Geomorphology*, <https://doi.org/10.1016/B978-0-12-818234-5.00166-8>, 2021.

709 Jay, D. A., Leffler, K. and Degens, S.: Long-term evolution of Columbia River tides, *ASCE*  
710 *Journal of Waterway, Port, Coastal, and Ocean Engineering*, 137: 182-191; doi:  
711 10.1061/(ASCE)WW.1943-5460.0000082, 2011.

712 Johnson, F., White, C.J., van Dijk, A. et al. Natural hazards in Australia: floods. *Climatic Change*  
713 139, 21–35. <https://doi.org/10.1007/s10584-016-1689-y>, 2016.

714 Jongman B., Ward P. J., Aerts J. C. J. H.: Global exposure to river and coastal flooding: Long term  
715 trends and changes. *Global Environmental Change*, 22(4): 823-35, 2012.

716 Kästner, K., Hoitink, A. J. F., Torfs, P. J. J. F., Deleersnijder, E., & Ningsih, N. S.: Propagation of  
717 tides along a river with a sloping bed. *Journal of Fluid Mechanics*, 872, 39–73.  
718 <https://doi.org/10.1017/jfm.2019.331>, 2019.

719 Kukulka, T. and Jay, D.A.: Impacts of Columbia River discharge on salmonid habitat: 1. A  
720 nonstationary fluvial tidal model. *Journal of Geophysical Research* v108 No. C9,  
721 doi:10.1029/2002JC001382, 2003a.

722 Kukulka, T. and Jay, D. A.: Impacts of Columbia River discharge on salmonid habitat: 2. Changes  
723 in shallow-water habitat. *Journal of Geophysical Research* v108 No. C9,  
724 doi:10.1029/2002JC001829, 2003b.

725 Lanzoni, S., and Seminara, G.: On tide propagation in convergent estuaries, *J. Geophys. Res.*, 103,  
726 30,793–30,812, 1998.

727 Munchow, A. K., Masse, A. K. & Garvine, R. W.: Astronomical and nonlinear tidal currents in a  
728 coupled estuary shelf system. *Continental Shelf Research* 12, 471-498, 1992.

729 Nicholls, R.J., Wong, P.P., Burkett, V.R., Codignotto, J.O., Hay, J.E., McLean, R.F., Ragoonaden,  
730 S., and Woodroffe C.D.: Coastal systems and low-lying areas. *Climate Change 2007:*  
731 *Impacts, Adaptation and Vulnerability. Contribution of Working Group II to the Fourth*  
732 *Assessment Report of the Intergovernmental Panel on Climate Change*, M.L. Parry, O.F.  
733 Canziani, J.P. Palutikof, P.J. van der Linden and C.E. Hanson, Eds., Cambridge University  
734 Press, Cambridge, UK, 315-356, 2007.

735 Olsen Associates Inc.: Calibration of a Delft3D model for Bald Head Island and the Cape Fear  
736 River entrance phase 1, 6114, 2012.

737 Orton, P., Georgas, N., Blumberg, A., and Pullen, J.: Detailed modeling of recent severe storm  
738 tides in estuaries of the New York City region, *J. Geophys. Res.*, 117, C09030,  
739 doi:10.1029/2012JC008220, 2012.

740 Orton, P. M., Hall, T. M., Talke, S.A., Blumberg, A.F., Georgas, N., and Vinogradov, S.: A  
741 validated tropical-extratropical flood hazard assessment for New York Harbor. *J. Geophys.*  
742 *Res. Oceans*, 121, 8904–8929, doi:https://doi.org/10.1002/2016JC011679, 2016.

743 Pareja-Roman, L. F., Chant, R. J., & Sommerfield, C. K.: Impact of historical channel deepening  
744 on tidal hydraulics in the Delaware Estuary. *Journal of Geophysical Research: Oceans*, 125,  
745 e2020JC016256. <https://doi.org/10.1029/2020JC016256>, 2020.

746 Parker, B. B.: The relative importance of the various nonlinear mechanisms in a wide range of  
747 tidal interactions. In: *Progress in Tidal Hydrodynamics*, Ed. by B. B. Parker, JohnWiley, pp.  
748 237-268, 1991.

749 Prandle, D., and Rahman, M.: Tidal response in estuaries. *Journal of Physical Oceanography*,  
750 10(10), 1552–1573, 1980.

751 Ralston, D. K., Talke, S., Geyer, W. R., Al-Zubaidi, H. A. M., & Sommerfield, C. K.: Bigger tides,  
752 less flooding: Effects of dredging on barotropic dynamics in a highly modified estuary.  
753 *Journal of Geophysical Research: Oceans*, 124, 196–211.  
754 <https://doi.org/10.1029/2018JC014313>, 2019.

755 Ralston, D. K., Warner, J. C., Geyer, W. R., and Wall, G. R.: Sediment transport due to extreme  
756 events: The Hudson River estuary after tropical storms Irene and Lee, *Geophys. Res. Lett.*,  
757 40, 5451– 5455, doi:10.1002/2013GL057906, 2013.

758 Savenije, H. H. G.: Analytical expression for tidal damping in alluvial estuaries, *J Hydraul Eng-*  
759 *Asce*, 124(6), 615–618, 1998.

760 Savenije, H. H. G., Toffolon, M., Haas, J., and Veling, E. J. M.: Analytical description of tidal  
761 dynamics in convergent estuaries, *J. Geophys. Res.*, 113, C10025,  
762 doi:10.1029/2007JC004408, 2008.

763 Shen, J., and Gong, W.: Influence of model domain size, wind directions and Ekman transport on  
764 storm surge development inside the Chesapeake Bay: A case study of extratropical cyclone  
765 Ernesto, 2006. *Journal of Marine Systems*, 75(1-2), 198–215.  
766 <http://doi.org/10.1016/j.jmarsys.2008.09.001>, 2009.

767 Shen, J., Wang, H., Sisson, M., and Gong, W.: Storm tide simulation in the Chesapeake Bay using  
768 an unstructured grid model. *Estuarine, Coastal and Shelf Science*, 68(1), 1–16.  
769 <http://doi.org/10.1016/j.ecss.2005.12.018>, 2006.

770 Talke, S. A., Familkhalili, R., and Jay, D. A.: The influence of channel deepening on tides, river  
771 discharge effects, and storm surge. *Journal of Geophysical Research: Oceans*, 126,  
772 e2020JC016328. <https://doi.org/10.1029/2020JC016328>, 2021.

773 Talke, S. A and Jay, D. A.: Changing tides: The role of natural and anthropogenic factors. *Annual*  
774 *Review of Marine Science*, <https://doi.org/10.1146/annurev-marine-010419-010727>, 2020.

775 Talke, S. A., Orton, P. and Jay, D. A.: Increasing storm tides in New York Harbor, 1844–2013,  
776 *Geophys. Res. Lett.*, 41, 3149–3155, doi:10.1002/2014GL059574, 2014.

777 Toffolon, M., and Savenije, H. H.: Revisiting linearized one-dimensional tidal propagation, *J.*  
778 *Geophys. Res.*, 116, C07007, doi:10.1029/2010JC006616, 2011.

779 van Oldenborgh, G. J., van der Wiel, K., Sebastian, A., Singh, R., Arrighi, J., Otto, F., et al.:  
780 Attribution of extreme rainfall from Hurricane Harvey, August 2017. *Environmental*  
781 *Research Letters*, 12, 124009, 2017.

782 Wahl, T., Jain, S., Bender, J., Meyers, S. D., and Luther, M. E.: Increasing risk of compound  
783 flooding from storm surge and rainfall for major US cities, *Nat. Clim. Change*, 5(12), 1093–  
784 1097, doi:10.1038/NCLIMATE2736, 2015.

785 Wang, S. Y. S., Zhao, L., Yoon, J. H., Klotzbach, P., & Gillies, R. R.: Attribution of climate effects  
786 on Hurricane Harvey’s extreme rainfall in Texas. *Environmental Research Letters*, 13.  
787 <https://doi.org/10.1088/1748-9326/aabb85>, 2018.

788 Winterwerp J. C., Wang Z. B., van Braeckel, A., van Holland, G., Kösters, F.: Man-induced regime  
789 shifts in small estuaries—II: a comparison of rivers. *Ocean Dyn.* 63:1293–306, 2013.

790 Wong, P. P., Losada, I. J., Gattuso, J. P., Hinkel, J., Khattabi, A., McInnes, K. L., Saito, Y., and  
791 Sallenger, A.: Coastal systems and low-lying areas, in *Climate Change: Impacts, Adaptation,*  
792 *and Vulnerability, Part A: Global and Sectoral Aspects, Contribution of Working Group II*  
793 *to the Fifth Assessment Report of the Intergovernmental Panel on Climate Change*, edited  
794 by C. B. Field et al., pp. 361–409, Cambridge Univ. Press, Cambridge, U. K., 2014.

795 Zheng, F., Westra, S., Leonard, M., Sisson, S.A.: Modeling dependence between extreme rainfall  
796 and storm surge to estimate coastal flooding risk. *Water Resour. Res.* 2014, 50, 2050–2071,  
797 2014.

798 Zscheischler, J., Westra, S., van den Hurk, B. J. J. M. et al.: Future climate risk from compound  
799 events. *Nature Clim Change* 8, 469–477, <https://doi.org/10.1038/s41558-018-0156-3>, 2018.